

Nobeyama Millimeter Array Observations of the Nuclear Starburst of M 83: A GMA Scale Correlation between Dense Gas Fraction and Star Formation Efficiency

Kazuyuki MURAOKA,¹ Kotaro KOHNO,² Tomoka TOSAKI,¹ Nario KUNO,¹
 Kouichiro NAKANISHI,¹ Toshihiro HANDA,² Kazuo SORAI,³ Sumio ISHIZUKI,⁴
 and Takeshi OKUDA,⁴

¹*Nobeyama Radio Observatory, Minamimaki, Minamisaku, Nagano 384-1305*
kmuraoka@nro.nao.ac.jp

²*Institute of Astronomy, The University of Tokyo, 2-21-1 Osawa, Mitaka, Tokyo 181-0015*

³*Division of Physics, Graduate School of Science, Hokkaido University, Sapporo 060-0810*

⁴*National Astronomical Observatory of Japan, 2-21-1 Osawa, Mitaka, Tokyo 181-8588*

(Received ; accepted)

Abstract

We present aperture synthesis high-resolution ($\sim 7'' \times 3''$) observations in CO($J = 1 - 0$) line, HCN($J = 1 - 0$) line, and 95 GHz continuum emission toward the central (~ 1.5 kpc) region of the nearby barred spiral galaxy M 83 with the Nobeyama Millimeter Array. Our high-resolution CO($J = 1 - 0$) mosaic map depicts the presence of molecular ridges along the leading sides of the stellar bar and nuclear twin peak structure. On the other hand, we found the distribution of the HCN($J = 1 - 0$) line emission which traces dense molecular gas ($n_{\text{H}_2} > \text{a few} \times 10^4 \text{ cm}^{-3}$) shows nuclear single peak structure and coincides well with that of the 95 GHz continuum emission which traces massive starburst. The peaks of the HCN($J = 1 - 0$) line and the 95 GHz continuum emission are not spatially coincident with the optical starburst regions traced by the HST V-band image. This suggests the existence of deeply buried ongoing starburst due to strong extinction ($A_V \sim 5$ mag) near the peaks of the HCN($J = 1 - 0$) line and the 95 GHz continuum emission. We found that the HCN($J = 1 - 0$)/CO($J = 1 - 0$) intensity ratio $R_{\text{HCN/CO}}$ correlates well with extinction-corrected SFE in the central region of M 83 at a resolution of $7''.5$ (~ 160 pc). This suggests that SFE is controlled by dense gas fraction traced by $R_{\text{HCN/CO}}$ even on a Giant Molecular cloud Association (GMA) scale. Moreover, the correlation between $R_{\text{HCN/CO}}$ and the SFE in the central region of M 83 seems to be almost coincident with that of the Gao & Solomon (2004a) sample. This suggests that the correlation between $R_{\text{HCN/CO}}$ and the SFE on a GMA (~ 160 pc) scale found in M 83 is the origin of the global correlation on a few kpc

scale shown by Gao & Solomon (2004a).

Key words: galaxies: ISM—galaxies: starburst—galaxies: individual (M 83; NGC 5236)

1. Introduction

Star formation is one of the most fundamental processes of the evolution of galaxies. Stars are formed by the contraction of molecular interstellar medium (ISM), and then a new ISM containing heavy element is dispersed into interstellar space by stellar wind and supernova explosions when stars end their lives. By repeating these processes, ISM, galaxies, and the Universe evolve. Therefore, the physics of star formation is very important in the understanding of the evolution of galaxies.

In the central regions of disk galaxies, we often find intense star-formation activities (e.g., Ho et al. 1997) where not only the star formation rate (SFR) but also the star formation efficiency (SFE; Young et al. 1996), which is an intensive parameter defined as the fraction of the SFR surface density in the surface mass density of molecular gas, are also enhanced. These star formation activities in central regions of galaxies are different from a simply scaled-up version of that in the disk region, and it is referred to as starburst (Kennicutt 1998b). The nuclear starburst is prominent not only because they show high SFR but also because they show elevated SFE. Therefore, for understanding the nuclear starburst we should reveal what causes the high SFE star formation.

It is essential to study *dense* molecular gas, because stars are formed from the dense cores of molecular clouds. In fact, recent studies of the dense molecular medium in galaxies based on the observations in the $\text{HCN}(J = 1 - 0)$ emission, a dense molecular gas tracer ($n_{\text{H}_2} > \text{a few } \times 10^4 \text{ cm}^{-3}$) due to its large dipole moment ($\mu_{\text{HCN}} = 3.0$ Debye, whereas $\mu_{\text{CO}} = 0.1$ Debye), demonstrate the intimate connection between dense molecular gas and massive star formation in galaxies. After the pioneer work by Solomon et al. (1992), a tight correlation between the $\text{HCN}(J = 1 - 0)$ intensity and FIR continuum luminosities has been shown among many galaxies including nearby ones (Gao & Solomon 2004a, Gao & Solomon 2004b), and high redshift quasar host galaxies (Carilli et al. 2005, Wu et al. 2005), although some deviations from the correlation are reported toward extreme environments (Riechers et al. 2007; Graciá-Carpio et al. 2008, Kohno et al. 2008a). A spatial coincidence between dense molecular gas traced by the $\text{HCN}(J = 1 - 0)$ emission and massive star-forming regions was also reported (Kohno et al. 1999, Shibatsuka et al. 2003). In addition, Gao & Solomon (2004a) reported that $\text{HCN}(J = 1 - 0)/\text{CO}(J = 1 - 0)$ integrated intensity ratio in the brightness temperature scale, hereafter $R_{\text{HCN/CO}}$, correlates well with SFE. This suggests that SFE is controlled by the fraction of dense molecular gas to the total amount of molecular contents traced by $R_{\text{HCN/CO}}$

(e.g., Solomon et al. 1992, Kohno et al. 2002a, Shibatsuka et al. 2003, Gao & Solomon 2004a).

However, these previous reports on the relationship between dense gas fraction and SFE are derived from coarse spatial resolution ($> 30''$) data of moderately distant galaxies ($D > 10$ Mpc). It means the results show a correlation on global scales of galaxies. In our Galaxy, a massive star-forming region is associated with the giant molecular clouds (GMCs) or their associations (giant molecular associations; GMAs). A typical scale of a GMC is a few 10 pc (Scoville & Sanders 1987) and that of a GMA is a few 100 pc. Therefore, we should investigate a correlation between dense gas fraction and SFE on this scale. To address this issue, observations with high-angular resolution of the central region of nearby galaxies are required.

In this paper, we present CO($J = 1 - 0$), HCN($J = 1 - 0$), and 95 GHz continuum observations toward the central regions of M 83 (NGC 5236) using the Nobeyama Millimeter Array (NMA). M 83 is a nearby, face-on, barred, grand-design spiral galaxy hosting an intense starburst at its center. The distance to M 83 is estimated to be 4.5 Mpc (Thim et al. 2003); therefore, $1''$ corresponds to 22 pc. We can then discuss the relation between $R_{\text{HCN/CO}}$ and the SFE at the center of M 83 on a GMA scale with a few arcsec resolution observations, which can be accomplished with the NMA. The high-resolution ($\leq 23'' \sim 500$ pc) CO line observations of the central region of M 83 have been performed repeatedly with various telescopes and in various transitions. We summarized them in table 1. For example, Handa et al. (1990) mapped the distribution of CO($J = 1 - 0$) emission for the center and bar at a resolution of $16''$ using the NRO 45-m telescope. They observed a large concentration of molecular gas in the nucleus and an extended ridge along the major axis of the bar. Ishizuki (1993) reported the CO($J = 1 - 0$) observation toward the center with the NMA. The distribution of CO($J = 1 - 0$) emission shows twin peak structure at the nucleus. Sakamoto et al. (2004) performed CO($J = 3 - 2$) and CO($J = 2 - 1$) emission observations toward the center and the bar using the Submillimeter Array (SMA). Their CO maps revealed two gas ridges on the leading side of the stellar bar and a nuclear gas ring of ~ 300 pc in diameter. The distribution of CO($J = 3 - 2$) emission is not coincident with the nuclear starburst, which is depicted by a three-color composite image made from *HST*/WFPC2 data, F300W, F547M, and F814W. The authors mentioned that the nuclear starburst in M 83 is lopsided, mostly on the receding side (south) of the dynamical center.

It is difficult to estimate the star formation activity accurately in the central starburst region because of strong extinction. Harris et al. (2001) presented a photometric catalog of 45 massive star clusters in the nuclear starburst region of M 83, observed with *HST*/WFPC2. They revealed that the ages of star clusters in the central 300 pc are younger than 10 Myr old, and the cluster age distribution has an extremely sharp peak at 5 – 7 Myr. However, the cluster ages in the north side of the nucleus are unknown since no clusters were found due to strong extinction by dust. They also mentioned the original starburst had started at the southern end of the nuclear starburst region, and propagated northward. The propagation of star formation

Table 1. Previous high-resolution CO observations of M 83.

Transition	Authors	Telescope	map size	resolution
J=1-0	Handa et al. (1990)	NRO 45-m	$3'.5 \times 1'$	$16''$
	Ishizuki (1993)	NMA	$1'.1 \times 1'.1$	$12'' \times 6''$
	Handa et al. (1994)	NMA	$1'.1 \times 1'.1$	$12'' \times 6''$
	Kuno et al. (2007)	NRO 45-m	$6' \times 6'$	$16''$
	This work	NMA	$2' \times 1'$	$7'' \times 3''$
J=2-1	Wall (1991)	JCMT 15 m		$22''$
	Israel & Baas (2001)	JCMT 15 m	$1'.2 \times 2'$	$21''$
	Lundgren et al. (2004)	SEST 15 m	$10' \times 10'$	$23''$
	Sakamoto et al. (2004)	SMA	$1'.5 \times 1'$	$3''.8 \times 2''.5$
J=3-2	Wall (1991)	CSO 10 m		$22''$
	Petitpas & Wilson (1998)	JCMT 15 m	$0'.7 \times 0'.7$	$14''$
	Israel & Baas (2001)	JCMT 15 m	$1'.2 \times 1'.7$	$14''$
	Dumke et al. (2001)	SMTO 10 m	$2' \times 2'$	$22''$
	Sakamoto et al. (2004)	SMA	$0'.6 \times 0'.6$	$3''.1 \times 1''.5$
	Bayet et al. (2006)	CSO 10 m	$4'.5 \times 2'$	$22''$
	Muraoka et al. (2007)	ASTE 10 m	$5' \times 5'$	$22''$
J=4-3	Petitpas & Wilson (1998)	JCMT 15 m	$0'.6 \times 0'.5$	$11''$
	Israel & Baas (2001)	JCMT 15 m	$0'.5 \times 0'.5$	$11''$

is also reported by Ryder et al. (2005) and by Houghton & Thatte (2008), who quantify the age gradient better using near-IR data.

To the north side of the nucleus, the $H\alpha/H\beta$ ratio is higher than that to the south side (see figure 4 in Harris et al. 2001). This means that dust extinction to the north side is stronger than that to the south side. The strong dust extinction indicates the existence of huge amounts of dust and molecular gas. In addition, the extinction on the north side has not yet been accurately estimated since it is too strong, and several authors suggests the existence of a highly-obscured nuclear starburst (Ryder et al. 2005, Fathi et al. 2008, Houghton & Thatte 2008). Therefore, it is necessary to evaluate the strength of extinction to investigate the relationship between molecular gas and true star formation in the central region of M 83.

The goals of this paper are: (1) to obtain distributions of total molecular gas and dense

molecular gas through CO($J = 1 - 0$) line and HCN($J = 1 - 0$) line emission in the central 1.5 kpc region of M 83 with a spatial resolution of ~ 100 pc, (2) to evaluate the extinction and reveal its distribution, and to obtain the extinction-corrected SFR and SFE. (3) to examine the correlation between dense gas fraction traced by $R_{\text{HCN/CO}}$ and the SFE on a GMA scale.

2. Observations and Data Reduction

Aperture synthesis observations in the CO($J = 1 - 0$) line, the HCN($J = 1 - 0$) line, and the 95 GHz continuum emission towards the central region (~ 1.5 kpc) of M 83 were carried out with the NMA during the periods from December 2003 to April 2004, and from December 2005 to April 2006. CO($J = 1 - 0$) line observations were made toward 3 adjacent field-of-views (FOVs) to make a mosaic of the center of the galaxy. HCN($J = 1 - 0$) line and 95 GHz continuum observations were made toward only a central FOV. Figure 1 shows the each FOV superposed on the V-band image obtained with the VLT (Comerón 2001).

The NMA consists of six 10-m antennas equipped with cryogenically cooled receivers employing Superconductor-Insulator-Superconductor mixers in double side band operation. Three antenna configurations (AB, C, and D) were used during the observations. The backend used was the Ultra Wide-Band Correlator (Okumura et al. 2000).

A radio source, J1337-129, was observed every ~ 20 minutes for amplitude and phase calibrations, and the passband shape of the system was determined from observations of a strong continuum source 3C 273. The flux density of J1337-129 was measured at several times during an observing run based on that of a quasar 3C 345. Its flux is determined by flux measurements of Saturn and Uranus. The overall error of the absolute flux scale was estimated to about $\pm 20\%$.

The raw visibilities were edited and calibrated using the NRO UVPROC-II package (Tsutsumi et al. 1997), and then final images were created using the IMAGR task in the NRAO AIPS package. For some spectral line analysis, data also have the continuum emission. In this case, we subtracted the continuum emission from the visibilities using the UVPROC-II task LCONT at first. We use the subtracted continuum emission in HCN($J = 1 - 0$) data as the 95 GHz continuum emission. Therefore, this flux is actually an average flux in two separated bands at 88.741 ± 0.5 GHz and 100.741 ± 0.5 GHz. Mosaic images in the CO($J = 1 - 0$) line were made using MIRIAD (Sault et al. 1995). Achieved sensitivities and spatial resolutions are summarized in table 2 and 3.

3. Results

3.1. Maps

Figure 2 shows an integrated intensity map and a velocity field in the CO($J = 1 - 0$) line, an integrated intensity map in the HCN($J = 1 - 0$) line, and a map of the 95 GHz continuum

Table 2. Observation parameters and results of M 83 with the NMA.

Observed line		CO($J = 1 - 0$)	HCN($J = 1 - 0$)
Rest frequency	[GHz]	115.271204	88.631604
Band width	[MHz]	512	1024
Band resolution	[MHz]	2	8
Velocity resolution	[km s ⁻¹]	5.2	27.1
Sideband		upper	lower
FOV	[$''$]	59	77
Number of FOVs		3 (mosaic)	1
Observed date		2003/12-2004/4	2005/12-2006/4
Synthesized beam size	[$''$]	7.2×3.4	7.1×3.1
Equivalent T_b	[K (Jy beam ⁻¹) ⁻¹]	3.76	7.15
rms noise (channel map)	[mJy beam ⁻¹]	85	7.2
	[mK]	320	51.5
rms noise (intensity map)	[Jy beam ⁻¹ km s ⁻¹]	2.7	0.52
	[K km s ⁻¹]	10.2	3.72
total flux within FOV	[Jy km s ⁻¹]	$2.4 \pm 0.1 \times 10^3$	60 ± 10
The central position of the FOV*			
R.A. (J2000)		$13^{\text{h}}37^{\text{m}}00^{\text{s}}.90$	
Decl. (J2000)		$-29^{\circ}51'56''.7$	

* Reference of the central position of the FOV — Jarrett et al. (2003)

Table 3. Summary of the 95 GHz continuum in M 83.

Synthesized beam	[$''$]	8.0×3.4
Equivalent T_b	[K (Jy beam ⁻¹) ⁻¹]	5.00
rms noise	[mJy beam ⁻¹]	0.85
	[mK]	4.25
total flux within FOV	[mJy]	30

Here, 95 GHz means a combination of 88.741 ± 0.5 GHz and 100.741 ± 0.5 GHz.

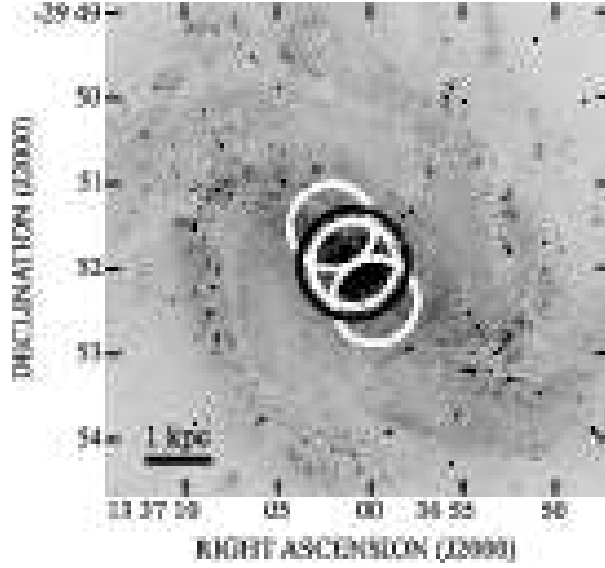


Fig. 1. Observed FOVs with the NMA superposed on a VLT V-band image of M 83 (Comerón 2001). White circles indicate the FOV for CO($J = 1 - 0$) observations, and a black circle indicates that for HCN($J = 1 - 0$) observations.

emission. Our high resolution CO($J = 1 - 0$) mosaic map depicts the presence of molecular ridges along the leading sides of the stellar bar and nuclear twin-peaks structure. This structure is seen in the previous studies in the CO($J = 1 - 0$) (Handa et al. 1994), and in the CO($J = 2 - 1$) and the CO($J = 3 - 2$) (Sakamoto et al. 2004). Strong non-circular motion along the molecular ridges was also detected in the velocity field. This strong non-circular motion is consistent well to that detected in the CO($J = 2 - 1$) velocity field (Sakamoto et al. 2004). The motion might play an important role in feeding large amount of molecular gas into the starburst nucleus. We determined the dynamical center from the CO velocity field using the AIPS task GAL (see table 4). We find the distributions of the HCN($J = 1 - 0$) line intensity, and the 95 GHz continuum flux are confined to a single peak, corresponding to the northern peak seen in the CO map. This means that dense molecular gas traced by the HCN($J = 1 - 0$) line and current star formation traced by the 95 GHz continuum emission are distributed only at north side of the center, although less dense molecular gas seen in the CO($J = 1 - 0$) line emission are widely distributed in the central region. The peak position of HCN($J = 1 - 0$) line intensity is consistent spatially with the youngest star clusters found by Harris et al. (2001) and Houghton & Thatte (2008).

Here, we summarized the positions of several peaks and nuclei determined from near-IR and our mm-wave data in figure 3 and table 4. The dynamical center determined from our CO velocity field is near the symmetry center of the outer K-band isophotes, whereas the visible nucleus (that is also the location of the K-band photometric peak in table 4) is offset from the dynamical center and the peaks of HCN($J = 1 - 0$) line intensity, 95 GHz continuum

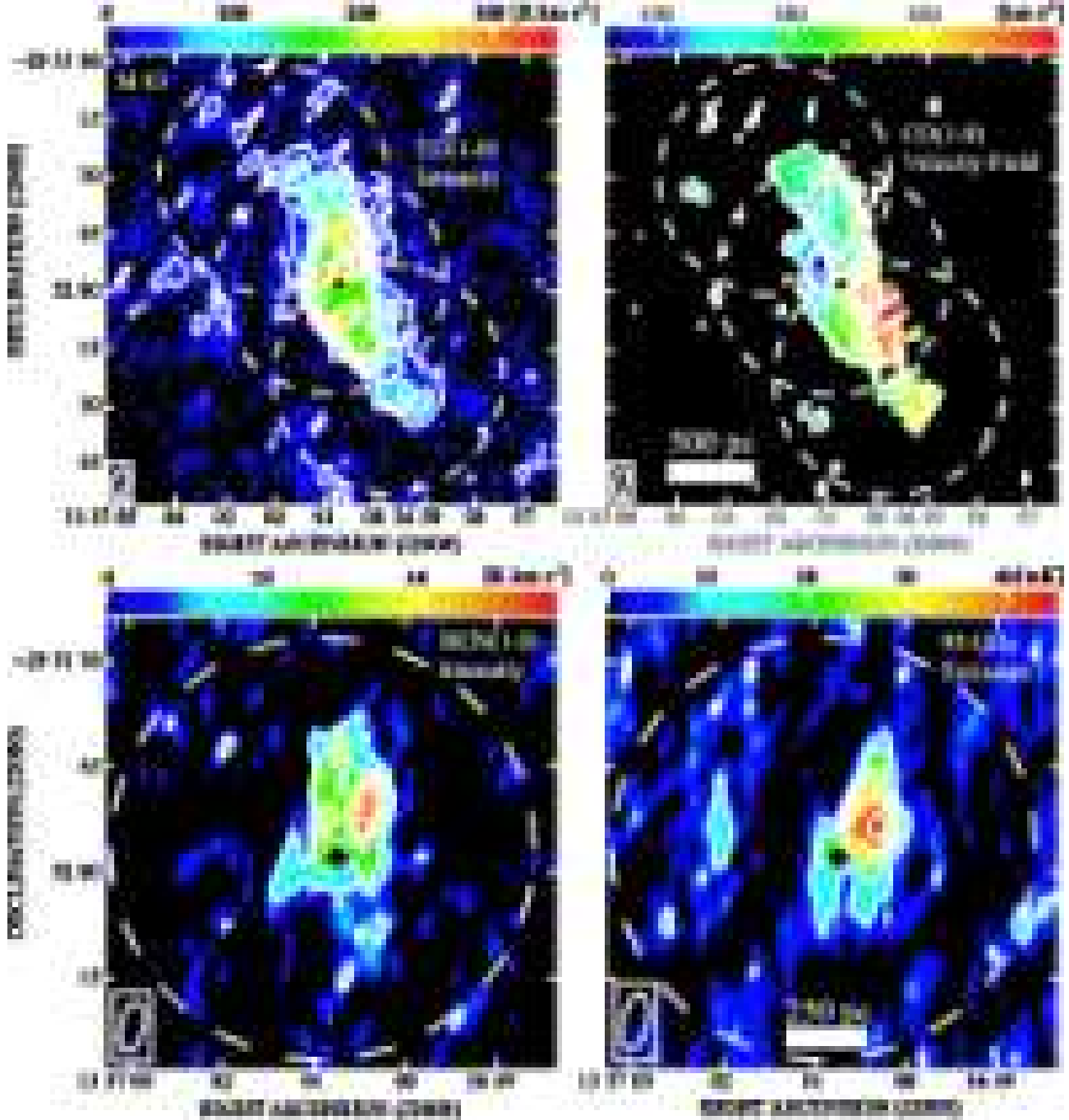


Fig. 2. (top left) Integrated intensity map in the CO($J=1-0$) emission in the central region of M 83. The central cross indicates the dynamical center determined from our CO velocity field, and dashed white circles indicate the FOVs of CO($J=1-0$) observations. The synthesized beam is shown in the lower left corner. The contour levels are 3, 6, 9, 12, 15, 21, 27, and 33 σ , where 1 $\sigma = 2.7 \text{ Jy beam}^{-1} \text{ km s}^{-1}$ or 10 K km s^{-1} . (top right) Velocity field measured in CO($J=1-0$). The contour levels are from 440 to 590 km s^{-1} with an interval of 10 km s^{-1} . (bottom left) Integrated intensity map in the HCN($J=1-0$) emission in the central region of M 83. The contour levels are 3, 6, 9, 12, and 15 σ , where 1 $\sigma = 0.52 \text{ Jy beam}^{-1} \text{ km s}^{-1}$ or 3.7 K km s^{-1} . (bottom right) Map of the 95 GHz continuum emission in the central region of M 83. The contour levels are 2, 4, 6, 8, 10 σ , where 1 $\sigma = 4.3 \text{ mK}$ or 0.85 mJy beam^{-1} .

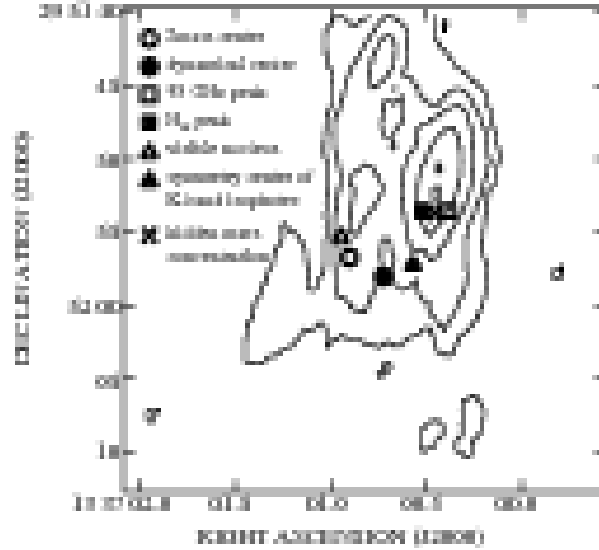


Fig. 3. Several peaks/nuclei in the central region of M 83 superposed on the $\text{HCN}(J = 1 - 0)$ integrated intensity map. The contour levels are the same as those in the bottom left of figure 2. The open circle shows infrared peak identified by the 2MASS image (the central position of the FOV), the filled circle shows the dynamical center, the open square shows the 95 GHz continuum peak, the filled square shows the peak of extinction-corrected $\text{H}\alpha$ luminosity (see section 4.1), the open triangle shows the visible nucleus, the filled triangle shows the symmetry center of the outer K-band isophotes, and the x mark shows the hidden mass concentration. See table 4 and text for details.

emission, and the extinction-corrected $\text{H}\alpha$ luminosity (see section 4.1). The position of the hidden mass concentration discussed in Díaz et al. (2006) and Houghton & Thatte (2008) seems to be coincident with the peaks of $\text{HCN}(J = 1 - 0)$ line intensity and the 95 GHz continuum emission, although the spatial resolutions of our mm-wave data ($7'' \times 3''$) are insufficient to make a detailed comparison.

We compare our $\text{HCN}(J = 1 - 0)$ map with that obtained by Helfer & Blitz (1997). The peak positions of the $\text{HCN}(J = 1 - 0)$ line emission are almost coincident between these two maps, whereas the flux values of the peak position are different. When our map was convolved to $12''.5 \times 4''.1$, which is the beam size of their map, the peak flux was measured as $12.5 \text{ Jy km s}^{-1}$. This value is about 30% lower than that of their data. It is unclear what causes such a significant discrepancy. Note that our $\text{HCN}(J = 1 - 0)$ line flux measured with the NMA is consistent well with that measured with the NRO 45-m telescope for central $22''$ region (see section 3.2).

3.2. Combining $\text{CO}(J = 1 - 0)$ data obtained with the NMA and the NRO 45-m

We found that the $\text{CO}(J = 1 - 0)$ spectrum at the center of M 83 obtained with the NMA is different from that obtained with the NRO 45-m telescope (Kuno et al. 2007) at the same resolution of $16''$ as shown in figure 4. This corresponds to missing flux of the interferometry, and we evaluated that the missing flux was $\sim 30 \%$. In order to correct the missing flux and

Table 4. Peaks/nuclei in the central region of M 83

R.A.	Decl.	description	reference
13 37 00.90	-29 51 56.7	2MASS, (the central position of the FOV)	Jarrett et al. (2003)
13 37 00.73	-29 51 57.9	dynamical center determined from CO velocity field	this work
13 37 00.38	-29 51 53.5	95 GHz continuum peak	this work
13 37 00.52	-29 51 53.5	peak of extinction-corrected H α luminosity	this work
13 37 00.95	-29 51 55.5	K-band photometric peak, visible nucleus	Thatte et al. (2000)
13 37 00.57	-29 51 56.9	the symmetry center of the outer K-band isophotes	Thatte et al. (2000)
13 37 00.46	-29 51 53.6	hidden mass concentration	Díaz et al. (2006)

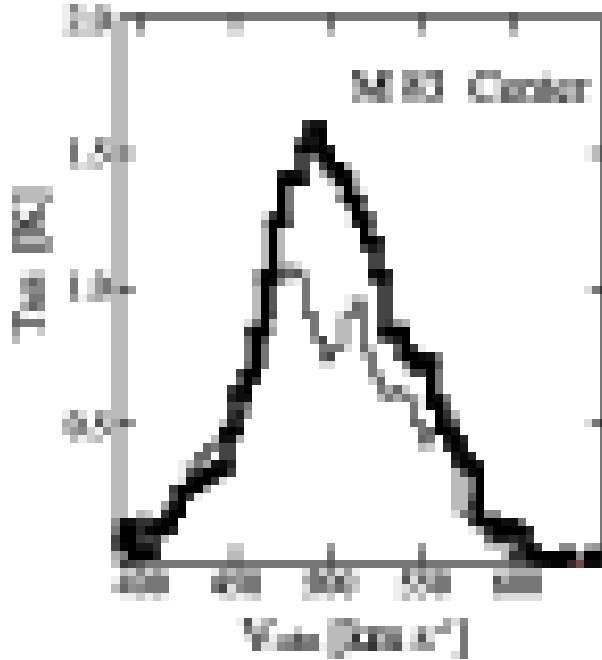


Fig. 4. CO($J = 1 - 0$) spectra at the center of M 83. The thick line corresponds to the spectrum obtained with the NRO 45-m (Kuno et al. 2007), and the thin line corresponds to that with the NMA (this work), which is convolved to the resolution of $16''$ to match the NRO 45-m data. The velocity resolutions of these spectra are both 5.2 km s^{-1} . The spectrum obtained with the NMA does not have a single peak but a twin-peak profile, and its intensity is $\sim 30\%$ lower than that obtained with the NRO 45-m.

obtain the true flux value in the CO($J = 1 - 0$) emission with the NMA, we combined the NMA CO($J = 1 - 0$) data with the NRO 45-m CO($J = 1 - 0$) data.

We employed the latest CO($J = 1 - 0$) data (Fukuhara et al. in prep.) obtained with the NRO 45-m using the On-the-Fly (OTF) method. The combination of two CO($J = 1 - 0$) data sets was performed using MIRIAD. Figure 5 shows a combined CO($J = 1 - 0$) image and an CO($J = 1 - 0$) image only with the NMA data. The results and specification of the combining are summarized in table 5. Compared to the NMA-only image, the flux was properly recovered

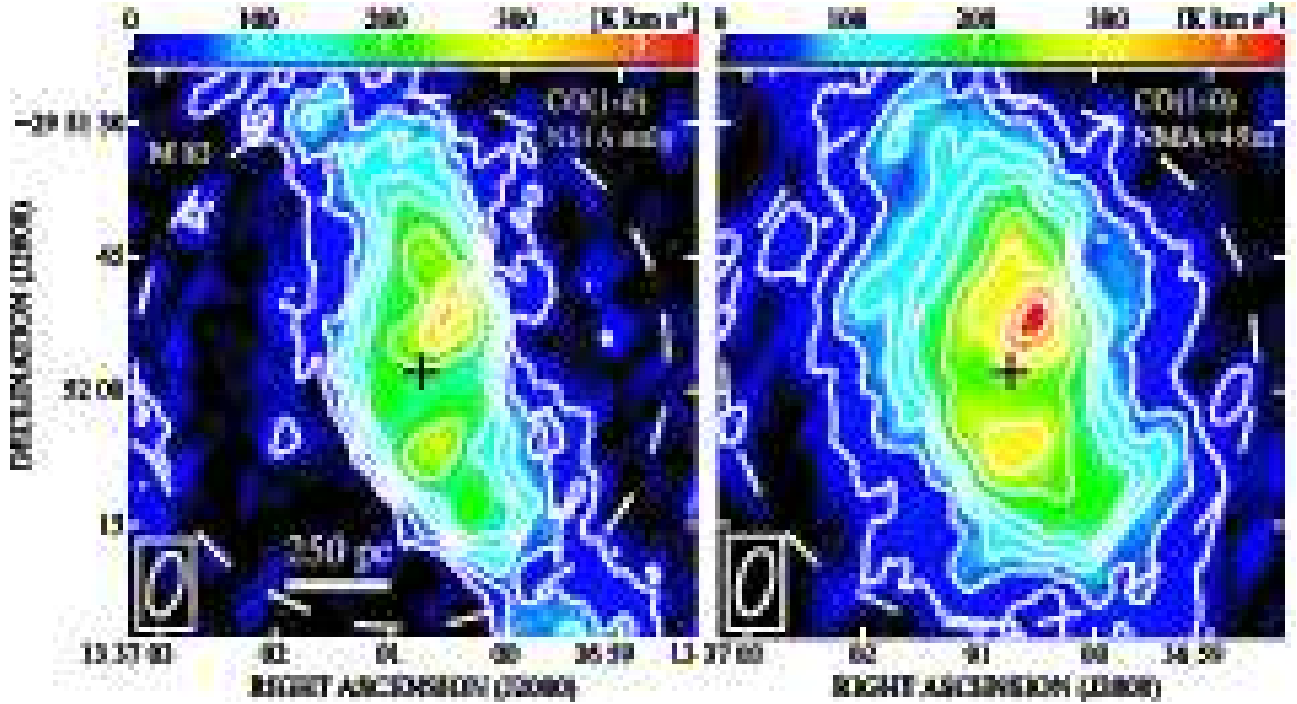


Fig. 5. (left) Integrated intensity map in the CO($J = 1 - 0$) before combining. The contour levels and the peak are the same as those in the top left of figure 2. The central cross indicates the dynamical center (see table 4). (right) Integrated intensity map in the CO($J = 1 - 0$) after combining. The contour levels are 3, 6, 9, 12, 15, 21, 27, 33, and 39 σ , where 1 $\sigma = 2.7 \text{ Jy beam}^{-1} \text{ km s}^{-1}$ or 10 K km s^{-1} .

at the center, and the CO-emitting area is enlarged in the combined image. That is, emission from diffuse components of molecular gas could be reproduced appropriately. The 45-m data made the resultant noise level lower and the synthesized beam size slightly wider. However, the overall structure at the center, such as the twin-peaks (or ring-like) is little affected by this combining process. For the HCN ($J = 1 - 0$) line, we did not combine the NMA data with single dish data. It is because we could not find any missing flux in the HCN($J = 1 - 0$) flux for the central $22''$ region. The flux obtained with the NMA, $38 \pm 3 \text{ Jy km s}^{-1}$, coincides well with that obtained with the NRO 45-m, $39 \pm 2 \text{ Jy km s}^{-1}$ (Hirota et al. in prep). This means that there is no significant diffuse component of HCN($J = 1 - 0$) emission. The difference in missing flux between CO($J = 1 - 0$) flux and HCN($J = 1 - 0$) flux suggests HCN emitting region is more restricted than CO emitting region. This is because HCN($J = 1 - 0$) emission is originated from dense molecular gas ($n_{\text{H}_2} > \text{a few } \times 10^4 \text{ cm}^{-3}$) associating with star-forming region, whereas CO($J = 1 - 0$) emission is originated from low-dense ($n_{\text{H}_2} \sim \times 10^2 \text{ cm}^{-3}$) component of molecular gas which is distributed ubiquitously.

We compare the combined CO($J = 1 - 0$) image with the NMA HCN($J = 1 - 0$) image in figure 6. This corresponds to the comparison between the total amount of the molecular gas and the dense molecular gas which will host star formation activity soon. The peak of the

Table 5. Parameters of CO($J = 1 - 0$) images before/after the 45-m data combine

		NMA only	NMA + 45-m
rms noise (channel map)	[mK]	320	273
	[mJy beam $^{-1}$]	85	80
rms noise (intensity map)	[K km s $^{-1}$]	10.2	8.53
	[Jy beam $^{-1}$ km s $^{-1}$]	2.7	2.5
Synthesized beam size	[$''$]	7.2×3.4	7.5×3.6
peak flux	[K km s $^{-1}$]	350	442
	[Jy beam $^{-1}$ km s $^{-1}$]	93	120
Equivalent T_b	[K (Jy beam $^{-1}$) $^{-1}$]	3.76	3.41

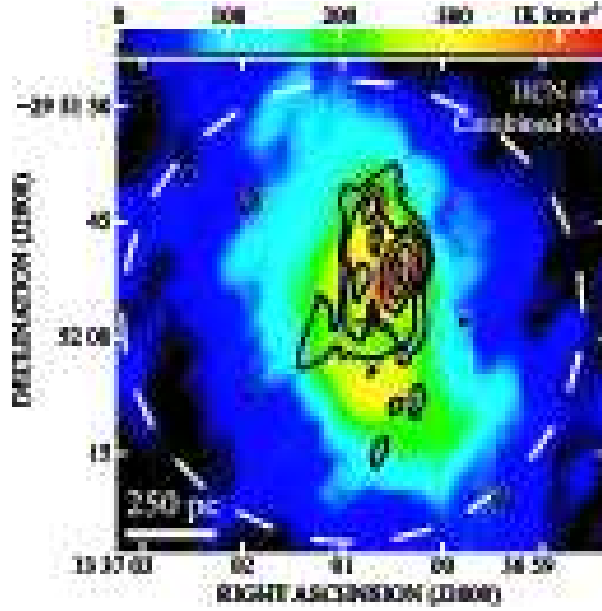


Fig. 6. Integrated intensity map in the HCN($J = 1 - 0$) emission (contour) superposed on an integrated intensity map of the combined CO($J = 1 - 0$) data (color). The central cross indicates the dynamical center. The contour levels of HCN($J = 1 - 0$) emission are the same as those of figure 2. The peak of HCN($J = 1 - 0$) intensity is almost coincident with the northern peak of CO($J = 1 - 0$) intensity, whereas little HCN($J = 1 - 0$) emission was seen at the southern peak of CO($J = 1 - 0$).

HCN($J = 1 - 0$) intensity is almost coincident with the northern peak of CO($J = 1 - 0$) intensity, whereas little HCN($J = 1 - 0$) emission was seen at the southern peak of CO($J = 1 - 0$). Smaller fraction of the dense gas at the southern peak suggests that this region may be in a post star formation phase.

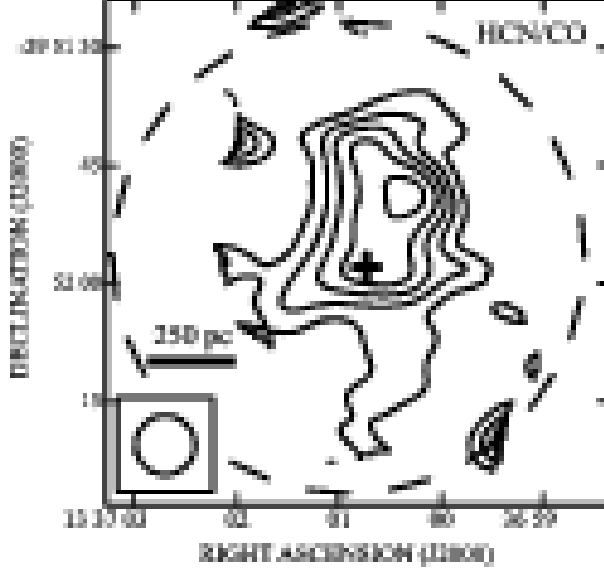


Fig. 7. Contour map of $R_{\text{HCN/CO}}$ in the central region of M 83. The central cross indicates the dynamical center. The contour levels are 0.02, 0.04, 0.06, 0.08, and 0.10, and the peak is 0.11. The peak of $R_{\text{HCN/CO}}$ resides northward with respect to the dynamical center. The spatial resolution of this map is $7''.5 \times 7''.5$, indicated by a circle in the lower left corner. The dashed circle represents the FOV of the CO image.

3.3. $\text{HCN}(J = 1 - 0)/\text{CO}(J = 1 - 0)$ intensity ratio $R_{\text{HCN/CO}}$

We made an intensity ratio map from the $\text{HCN}(J = 1 - 0)$ data and the combined $\text{CO}(J = 1 - 0)$ data. To improve the data quality and to adjust the beamsize we convolved the images to have the same $7''.5 \times 7''.5$ ($160 \text{ pc} \times 160 \text{ pc}$) resolution before calculating the ratio. The resultant $R_{\text{HCN/CO}}$ map is shown in figure 7. The peak of $R_{\text{HCN/CO}}$ value is 0.11 ± 0.01 . The region with high $R_{\text{HCN/CO}}$ is concentrated to the north side of the dynamical center of the galaxy. The high ratio region has an elongation southward toward the dynamical center.

3.4. Comparison with optical image

To compare our millimeter-wave images with an optical image obtained with the *HST*/WFPC2, we made the maps of the combined $\text{CO}(J = 1 - 0)$ intensity, the $\text{HCN}(J = 1 - 0)$ intensity, the 95 GHz continuum, and $R_{\text{HCN/CO}}$, respectively, superposed on the *HST* V-band image (F547M) obtained from *HST*/WFPC2 archival data. These maps are shown in figure 8. The V-band image shows the distribution of optically luminous young star clusters, which is referred to as “optical starburst.” The optical starburst region is distributed on the south side of the center, and is confined between the twin peaks in the $\text{CO}(J = 1 - 0)$ emission line. The distribution of the $\text{HCN}(J = 1 - 0)$ integrated intensity is shifted northward with respect to that of the optical starburst. Moreover, even the 95 GHz continuum, which is believed to trace current star formation as well as $\text{H}\alpha$, is also clearly shifted northward from the optical starburst region and the peak is close to that in the $\text{HCN}(J = 1 - 0)$ line. This means the

“optical starburst” seen in the V-band does not trace current star-forming region. The fact is also reported on the basis of near-IR imaging (Ryder et al. 2005, Houghton & Thatte 2008).

4. Discussion

4.1. Extinction in the central region of M 83

As described in the previous section, we found that the optical starburst region of M 83 is not spatially coincident with current star-forming region traced by the 95 GHz continuum. This spatial inconsistency is probably due to strong extinction. To confirm this possibility, we estimate the magnitude and distribution of extinction.

Some previous researches conclude that extinction at the center of M 83 is not small. Thatte et al. (2000) reported that V-band extinction A_V spreads from 0.5 to 9.2 mag in the central 12'' (~ 250 pc) region. Harris et al. (2001) reported that extinction to the north of the center ($\sim 15''$ or 330 pc) is stronger than that to the south. This suggests that A_V is different from place to place and it is very large. Therefore, we should estimate the A_V with enough accuracy.

To estimate the $H\alpha$ extinction, $A_{H\alpha}$, we use the $Pa\alpha$ emission. We employed an $H\alpha$ image obtained with the CTIO 1.5-m telescope (Meurer et al. 2006) and a $Pa\alpha$ image obtained with archival data of the *HST*/NICMOS camera (P.I. M. Rieke, Proposal I.D. 7218). The $Pa\alpha$ image is convolved to be the same resolution as that of the $H\alpha$, 1''.84, although the resolution of the $Pa\alpha$ image is 0''.15. Note that the FOV of the $Pa\alpha$ image is narrower than that of NMA observations.

We adopted a metallicity-dependent intrinsic ratio $H\alpha/Pa\alpha = 8.45$ in the assumption of electron temperature $T_e = 10000$ K for $n_e = 100 \text{ cm}^{-3}$ (Osterbrock & Ferland 2006). This means that without any extinction

$$L_{H\alpha, \text{corr}}/L_{Pa\alpha, \text{corr}} = 8.45, \quad (1)$$

where $L_{H\alpha, \text{corr}}$ means extinction-corrected $H\alpha$ luminosity, and $L_{Pa\alpha, \text{corr}}$ means that of $Pa\alpha$. From an extinction curve we used,

$$A_{H\alpha}/A_{Pa\alpha} = 6.0. \quad (2)$$

From combination of these two relations, we got formula to calculate $A_{H\alpha}$.

$$\begin{aligned} L_{H\alpha, \text{corr}}/L_{Pa\alpha, \text{corr}} &= (10^{A_{H\alpha}/2.5} L_{H\alpha, \text{obs}})/(10^{A_{Pa\alpha}/2.5} L_{Pa\alpha, \text{obs}}) \\ &= (10^{A_{H\alpha}/2.5} L_{H\alpha, \text{obs}})/(10^{A_{H\alpha}/15} L_{Pa\alpha, \text{obs}}) \\ &= 8.45. \end{aligned} \quad (3)$$

Since $L_{H\alpha, \text{obs}}$ and $L_{Pa\alpha, \text{obs}}$ can be calculated from each observed set of data, $A_{H\alpha}$ could be obtained.

Figure 9 shows the obtained $A_{H\alpha}$ map and an extinction-corrected $H\alpha$ luminosity map

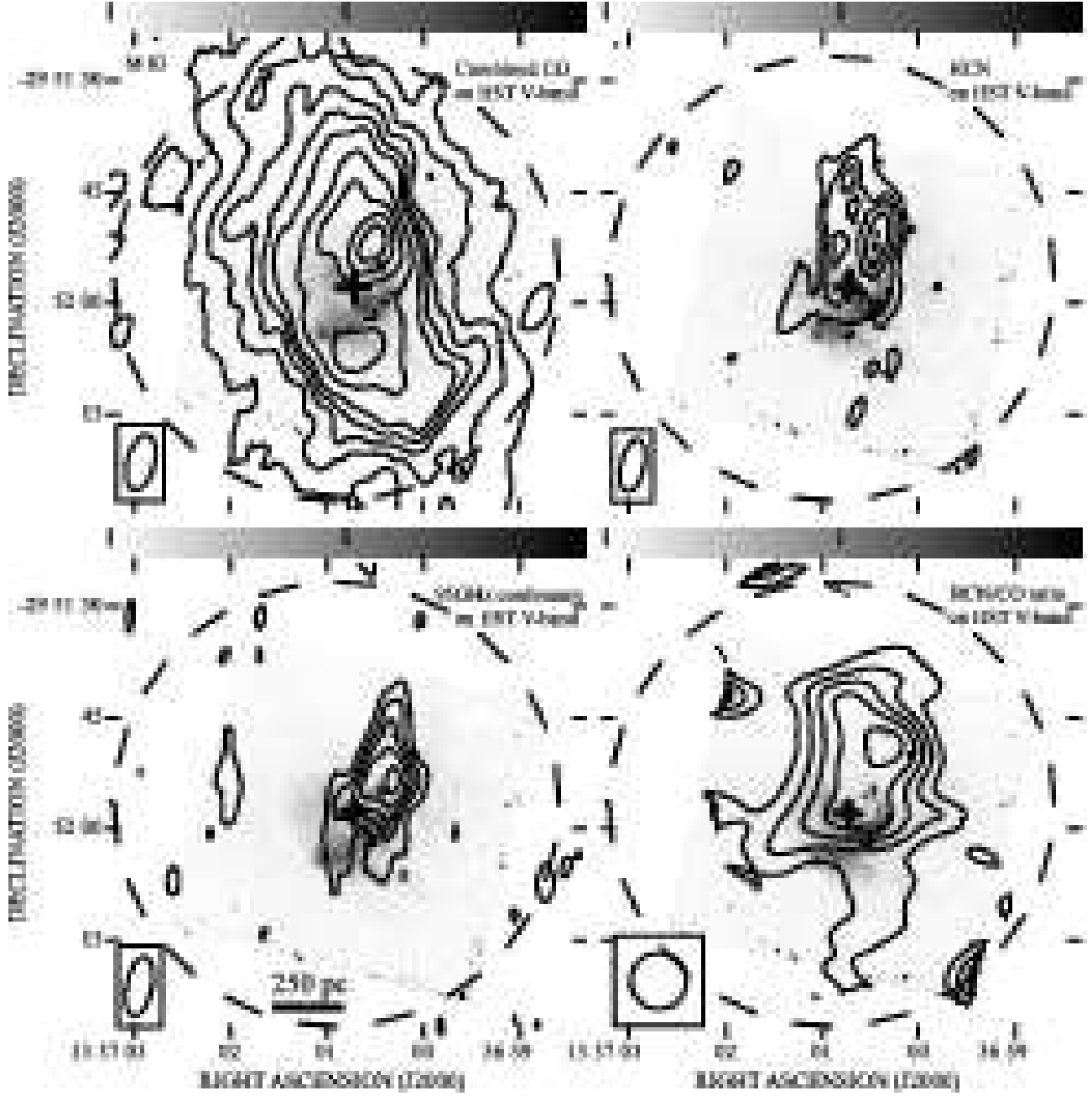


Fig. 8. (top left) Integrated intensity map of the combined CO($J=1-0$) (contour) superposed on the HST V-band (F547M) image (grey scale). The contour levels are the same as those in the right of figure 5. The central cross indicates the dynamical center. (top right) Integrated intensity map in the HCN($J=1-0$) (contour) superposed on the HST V-band image (grey scale). The contour levels are the same as those in the bottom left of figure 2. (bottom left) 95 GHz continuum image (contour) superposed on the HST V-band image (grey scale). The contour levels are the same as those in the bottom right of figure 2. (bottom right) $R_{\text{HCN}/\text{CO}}$ map (contour) superposed on the HST V-band image (grey scale). The contour levels are the same as those in figure 7.

for the central $20''$ region of M 83. The maximum $A_{\text{H}\alpha}$ is about 4 mag, and its location is almost coincident with the nuclear peak of the $\text{HCN}(J = 1 - 0)$ emission. $A_{\text{H}\alpha} \sim 4$ mag corresponds to $A_V \sim 5$ mag. Thus, the optical light is extinct by a factor of 100 around the $\text{HCN}(J = 1 - 0)$ peak. In addition, the peak of the extinction-corrected $\text{H}\alpha$ luminosity coincides well with those of the $A_{\text{H}\alpha}$ and the $\text{CO}(J = 1 - 0)$ line, the $\text{HCN}(J = 1 - 0)$ line, and the 95 GHz continuum emission. On the other hand, extinction is almost negligible to the south of the center. This inhomogeneous extinction shows why the optical starburst is clearly visible to the south of the center but almost invisible in the north side. This suggests the existence of deeply buried ongoing starburst with strong extinction, which is already reported by several authors (e.g., Ryder et al. 2005, Houghton & Thatte 2008), near the peaks in the $\text{HCN}(J = 1 - 0)$ line and the 95 GHz continuum emission.

4.2. Star formation rates at the center of M 83

In order to discuss the relationship between dense molecular gas and star formation, we estimate the SFR in the central $22''$ (~ 500 pc) region of M 83. We used various SFR indicators, i.e. our 95 GHz (3 mm) continuum emission, 5 GHz (6 cm) continuum emission, infrared (IR) luminosity, and extinction-corrected $\text{H}\alpha$ luminosity. All of them should be consistent when all corrections are applied properly.

4.2.1. SFR derived from thermal free-free emission flux

Continuum emission at 95 GHz is expected to be an extinction-free tracer of SFR. This is because continuum emission in this wavelength is dominated by thermal free-free emission, and is therefore directly converted to the Lyman photon rate (Condon 1992).

By assuming that the observed 95 GHz continuum is dominated by the thermal free-free emission, a Lyman continuum rate or $\text{H}\alpha$ luminosity can be evaluated by the following formula (Condon 1992, Kohno et al. 2008b),

$$L_{\text{H}\alpha} = 9.6 \times 10^{37} \left(\frac{D}{\text{Mpc}} \right)^2 \left(\frac{T_e}{10^4 \text{ K}} \right) \left(\frac{\nu}{\text{GHz}} \right)^{0.1} \left(\frac{S_{\text{thermal}}}{\text{mJy}} \right) \text{ erg s}^{-1} \quad (4)$$

where D is the distance to the galaxy, T_e is the electron temperature, ν is the frequency, and S_{thermal} is the flux density of the thermal free-free continuum emission. We assume that the observed 95 GHz continuum flux within the central $22''$ region of M 83, $S_{\text{thermal}} = 30$ mJy, is dominated by the thermal free-free continuum emission. Then, we derived $L_{\text{H}\alpha}(95 \text{ GHz}) = 9.2 \times 10^{40} \text{ erg s}^{-1}$. Using this $L_{\text{H}\alpha}(95 \text{ GHz})$, we can derive an SFR by adopting the relation between $\text{H}\alpha$ luminosity and SFR (Kennicutt 1998a, Kennicutt 1998b),

$$\text{SFR} = 7.9 \times 10^{-42} \left(\frac{L_{\text{H}\alpha}}{\text{erg s}^{-1}} \right) M_{\odot} \text{ yr}^{-1}. \quad (5)$$

The resultant SFR from our 95 GHz continuum flux is $0.73 \pm 0.21 M_{\odot} \text{ yr}^{-1}$. The error is estimated from the signal-to-noise(S/N) ratio of the 95 GHz continuum map.

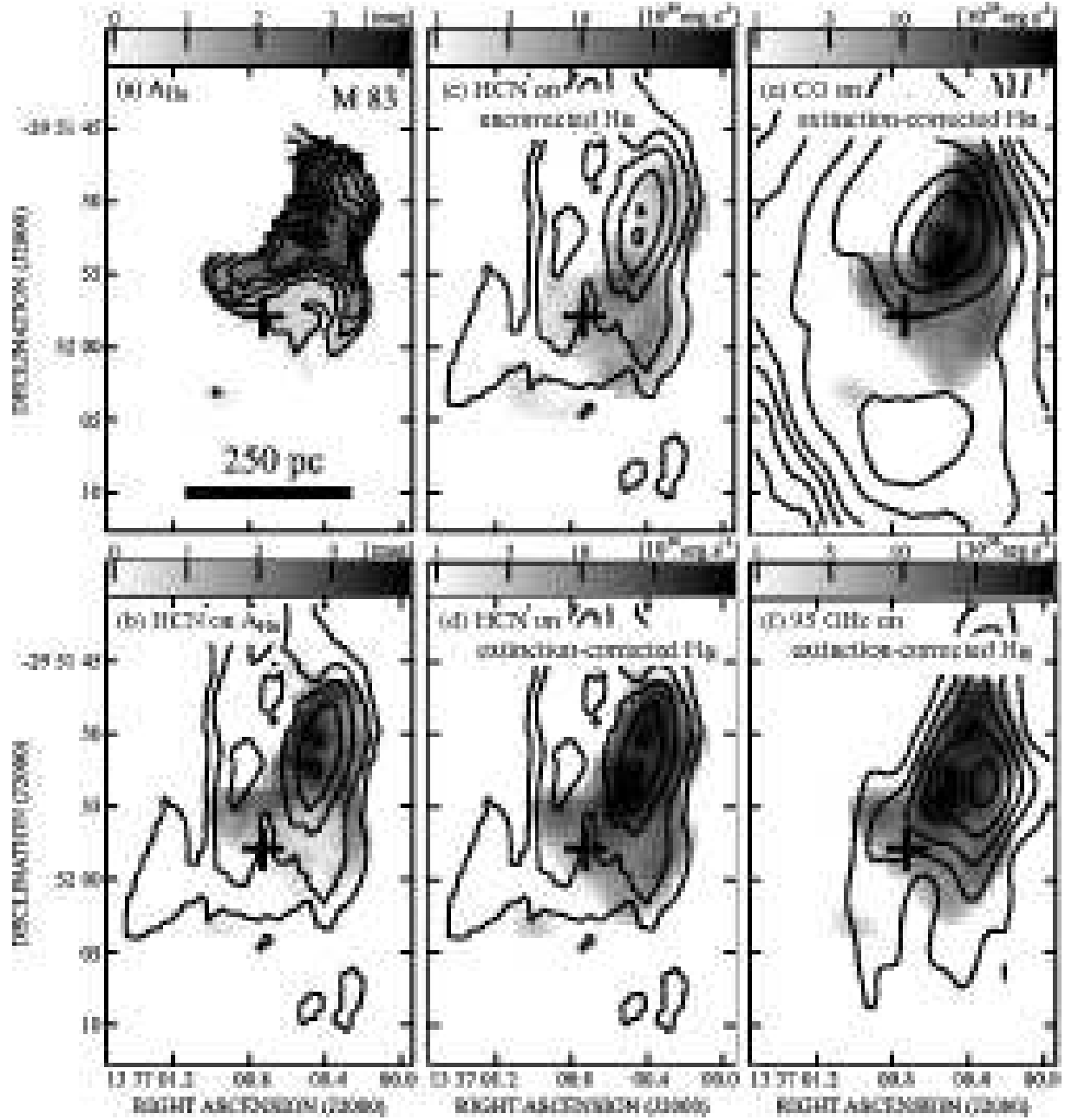


Fig. 9. (a) A map of extinction in $H\alpha$ emission. The contour levels are 0.5, 1.0, 1.5, 2.0, 2.5, 3.0, and 3.5 mag, and the peak is 3.9 mag. The central cross indicates dynamical center. (b) An integrated intensity map in the $\text{HCN}(J = 1 - 0)$ emission (contour) superposed on an extinction map of $H\alpha$ (grey scale). The contour levels are the same as those of figure 2. (c) An integrated intensity map in the $\text{HCN}(J = 1 - 0)$ emission (contour) superposed on an uncorrected $H\alpha$ luminosity map (grey scale). (d) An integrated intensity map in the $\text{HCN}(J = 1 - 0)$ emission (contour) superposed on an extinction-corrected $H\alpha$ luminosity map (grey scale). (e) An integrated intensity map of the combined $\text{CO}(J = 1 - 0)$ emission (contour) superposed on an extinction-corrected $H\alpha$ luminosity map (grey scale). The contour levels are the same as those of figure 2. (f) A map of the 95 GHz continuum emission (contour) superposed on an extinction-corrected $H\alpha$ luminosity map (grey scale). The contour levels are the same as those of figure 2.

4.2.2. SFRs derived from IR luminosity and non-thermal radio continuum flux

In order to evaluate the validity of the derived SFR from 95 GHz continuum flux, we computed the SFR from IR luminosity and 5 GHz radio continuum flux. According to Kennicutt (1998a), the SFR derived from IR luminosity within the central 22'' region is $0.37 M_{\odot} \text{ yr}^{-1}$, which is almost half the value of the SFR based on the 95 GHz continuum.

We then derived the SFR from 5 GHz radio continuum flux. Non-thermal radio luminosity is related to the observed radio continuum flux density as

$$L_{\text{non-thermal}} = 1.2 \times 10^{17} \left(\frac{D}{\text{Mpc}} \right)^2 \left(\frac{S}{\text{mJy}} \right) \left[1 - \left[1 + 10 \left(\frac{\nu}{\text{GHz}} \right)^{(0.1-\alpha)} \right]^{-1} \right] \text{W Hz}^{-1} \quad (6)$$

(Kohno et al. 2008b), where D is the distance, S the observed flux density at the frequency of ν , and α the non-thermal continuum spectral index (~ 0.8). This non-thermal radio luminosity is related to an SFR as

$$\text{SFR} = 8.2 \times 10^{-22} \left(\frac{\nu}{\text{GHz}} \right)^{\alpha} \left(\frac{L_{\text{non-thermal}}}{\text{W Hz}^{-1}} \right) M_{\odot} \text{ yr}^{-1} \quad (7)$$

(Jogee et al. 2005). From these equations and the 5 GHz radio continuum map produced by Neininger et al. (1993), we obtained the SFR of $0.73 \pm 0.15 M_{\odot} \text{ yr}^{-1}$ within the central 22'' region, which is the same value as the SFR based on the 95 GHz continuum.

4.2.3. SFR derived from extinction-corrected H α luminosity

SFR can be calculated from H α luminosity as shown in equation (5). However, the H α emission often suffers from extinction by interstellar dust. In fact, there is up to 4 mag of H α extinction in the central region of M 83 as described in the previous subsection.

Therefore, there is no doubt that appropriate correction of extinction is indispensable. Here we must verify what data should be used to correct extinction. Pa α seems to be very useful, but cannot cover the entire FOV of CO($J = 1 - 0$) and HCN($J = 1 - 0$) image.

Recently, the Spitzer/MIPS 24 μm image has begun to be employed for calibration of SFR (e.g. M 51; Calzetti et al. 2007). An archival MIPS 24 μm image (P00059, George, Rieke, Starburst activity in nearby galaxies) covers the entire disk of M 83, and the spatial resolution of the image is about 5''.7. The formula to calibrate H α luminosity using 24 μm image is as follows (Calzetti et al. 2007).

$$L_{\text{H}\alpha, \text{corr}} = L_{\text{H}\alpha, \text{obs}} + (0.031 \pm 0.006) L_{24\mu\text{m}} \text{ erg s}^{-1} \quad (8)$$

where $L_{\text{H}\alpha, \text{obs}}$ means observed H α luminosity, and $L_{24\mu\text{m}}$ means that of 24 μm . At the center of M 83, H α extinction derived from MIPS 24 μm image is about 3 mag at a resolution of 5''.7. Considering the difference in spatial resolution, the derived H α extinction from MIPS 24 μm image seems to be consistent with that from the Pa α image. Using equation (5), the resultant SFR from extinction-corrected H α is $0.24 \pm 0.05 M_{\odot} \text{ yr}^{-1}$ within the central 22'' region. This value is close to that from IR luminosity, but 3 times smaller than that from 95 GHz and 5 GHz continuum flux.

Table 6. Star formation rates from various indicators within the central 22'' region.

Indicator	SFR	Reference of emission data
95 GHz (3 mm) continuum	0.73 ± 0.21	This work
5 GHz (6 cm) continuum	0.73 ± 0.15	(1)
IR luminosity	0.37	(2)
extinction-corrected H α	0.24 ± 0.05	(3)

Reference —. (1) Neininger et al. (1993), (2) Kennicutt (1998a), (3) Meurer et al. (2006)

The SFRs derived from various indicators are summarized in table 6. It is unclear what causes such a significant discrepancy among these SFRs.

4.3. Comparison between $R_{\text{HCN/CO}}$ and SFE

4.3.1. Derivation of SFE

In order to compare the SFE in the central region directly with our $R_{\text{HCN/CO}}$ data, we need reliable SFR data with an adequate sensitivity and an adequate spatial resolution higher than 7''.5. For the IR luminosity data and the 5 GHz continuum data, their spatial resolutions ($\geq 10''$) are inadequate. In addition, our 95 GHz continuum data is unfavorable for comparing $R_{\text{HCN/CO}}$ since the area where 95 GHz continuum emission is detected in adequate S/N ratio (more than 5σ) is narrower than that of $R_{\text{HCN/CO}}$. Then, we use the SFR data based on the extinction-corrected H α luminosity using MIPS 24 μm data in order to calculate the SFE in the central region.

The SFE is calculated as follows,

$$\text{SFE} = \left(\frac{\Sigma_{\text{SFR}}}{M_{\odot} \text{ yr}^{-1} \text{ pc}^{-2}} \right) \left(\frac{\Sigma_{\text{H}_2}}{M_{\odot} \text{ pc}^{-2}} \right)^{-1} \text{ yr}^{-1}. \quad (9)$$

Σ_{SFR} is the surface mass density of SFR, and Σ_{H_2} is that of molecular gas. Σ_{H_2} is calculated as follows,

$$\Sigma_{\text{H}_2} = 2.89 \cos i \left(\frac{I_{\text{CO}(J=1-0)}}{\text{K km s}^{-1}} \right) M_{\odot} \text{ pc}^{-2}. \quad (10)$$

Here, the $N_{\text{H}_2}/I_{\text{CO}}$ conversion factor (X_{CO}) is assumed to be $1.8 \times 10^{20} \text{ cm}^{-2} (\text{K km s}^{-1})^{-1}$ (Dame et al. 2001). $I_{\text{CO}(J=1-0)}$ is derived from the combined CO($J = 1 - 0$) intensity map. Figure 10 shows the calibrated Σ_{SFR} map and the SFE map. Both maps are convolved to the resolution of $7''.5 \times 7''.5$ ($160 \text{ pc} \times 160 \text{ pc}$) to match $R_{\text{HCN/CO}}$ data. The peak value of the SFR is $\sim 4 \times 10^{-6} M_{\odot} \text{ yr}^{-1}$. The peak value of SFE (i.e. the site where most active star formation is supposed to occur) is $\sim 5 \times 10^{-9} \text{ yr}^{-1}$ and it is located north of the center. The highest SFE region is spatially coincident well with the highest SFR region.

4.3.2. $R_{\text{HCN/CO}}$ vs. SFE in M 83: correlation in a GMA scale

Here, we compare $R_{\text{HCN/CO}}$ with the SFE within the central 1 kpc region of M 83. Figure 11 shows the map of $R_{\text{HCN/CO}}$ superposed on that of SFE. The spatial correlation

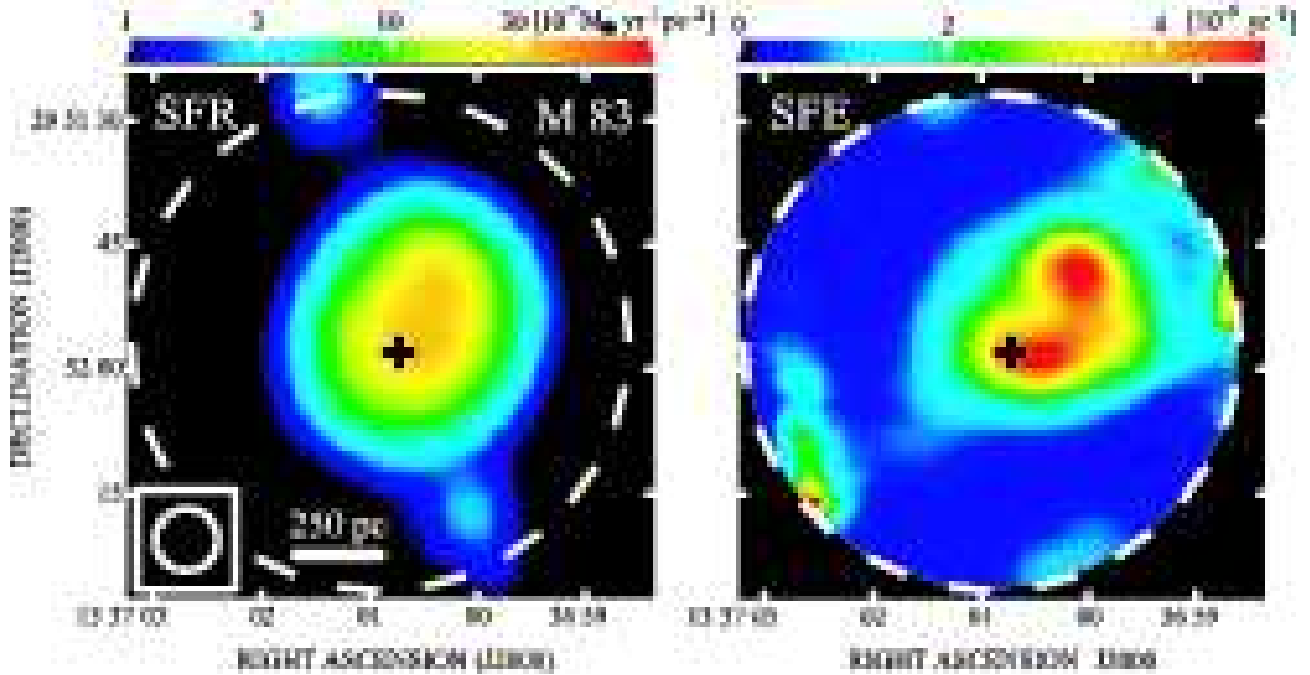


Fig. 10. (left) A map of the SFR in the central region of M 83 estimated from calibrated $H\alpha$ luminosity. The central cross indicates the dynamical center. The peak of the SFR is $4 \times 10^{-6} M_{\odot} \text{ yr}^{-1} \text{ pc}^{-2}$. The spatial resolution of this map is $7''.5 \times 7''.5$, indicated by a circle in the left corner. (right) A map of the SFE in the central region of M 83. The peak of the SFE is $5 \times 10^{-9} \text{ yr}^{-1}$, and it coincides well spatially with that of SFR.

between these two maps seems to be roughly good, but $R_{\text{HCN/CO}}$ map seems to trail the skirt toward the northeast. This skirt-like structure of $R_{\text{HCN/CO}}$ is not seen in the SFE map, and is coincident with the dust lane seen in the VLT V-band image (Comerón 2001).

In addition, we examine the correlation between $R_{\text{HCN/CO}}$ and the SFE. For the region where $R_{\text{HCN/CO}}$ exceeds 0.02, the values of $R_{\text{HCN/CO}}$ and the SFE are obtained for each separation of $3''.75$, which corresponds to half of the spatial resolution of each map. Figure 12 shows a plot of $R_{\text{HCN/CO}}$ vs. the SFE in each region. The correlation between $R_{\text{HCN/CO}}$ and the SFE is clearly seen.

These $R_{\text{HCN/CO}}$ correspond to the dense gas fraction in the central region of M 83 on a 160 pc (corresponding to GMA) scale. The dense gas fraction would be translated as the number of star-forming dense cores per unit gas mass. Then, the correlation derived between $R_{\text{HCN/CO}}$ means that an outbreak of extensive star formation (high-SFE star formation) such as the nuclear starburst requires the generation of a large number of star-forming dense cores within GMAs (e.g., Solomon et al. 1992, Kohno et al. 2002a, Shibatsuka et al. 2003, Gao & Solomon 2004a).

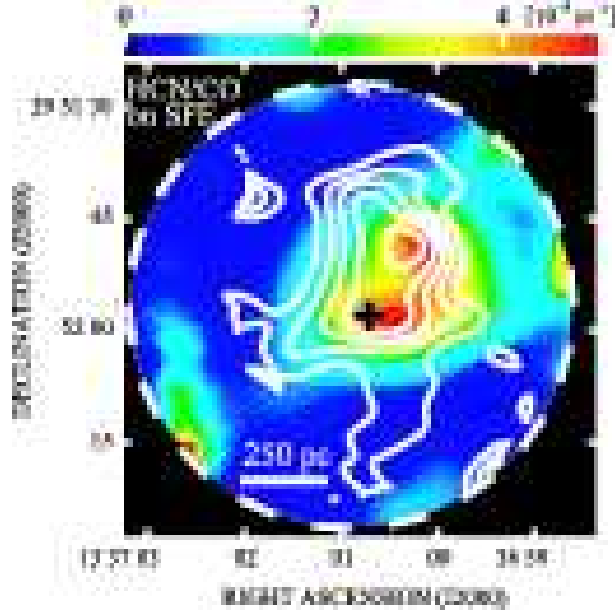


Fig. 11. A map of $R_{\text{HCN/CO}}$ (white contour) superposed on a map of the SFE in the central region of M 83 (color). The central cross indicates the dynamical center. The spatial correlation between these two maps seems to be roughly good. The contour levels are the same as those of figure 7.

4.3.3. $R_{\text{HCN/CO}}$ vs. SFE: comparison with a global scale correlation

We compare our results with that shown by Gao & Solomon (2004a). We converted the SFR in M 83, which is estimated from extinction-corrected $\text{H}\alpha$ luminosity, to the total IR (8 to 1000 μm) luminosity using the following formula (Kennicutt 1998a),

$$L_{\text{IR}} = 2.2 \times 10^{43} \left(\frac{\text{SFR}}{M_{\odot} \text{ yr}^{-1}} \right) \text{ erg s}^{-1}. \quad (11)$$

Then, we adapted the vertical axis of our $R_{\text{HCN/CO}}$ vs. SFE plot to that of figure 5a in Gao & Solomon (2004a). Figure 13 shows the composite of the $R_{\text{HCN/CO}}$ vs. SFE plot for the center of M 83 and for ULIRGs, LIRGs, and normal spirals (Gao & Solomon 2004a). The correlation between $R_{\text{HCN/CO}}$ and the SFE in the central region of M 83 almost seems to coincide with that of Gao & Solomon (2004a) sample. This suggests that the correlation between $R_{\text{HCN/CO}}$ and SFE on a GMA (~ 160 pc) scale found in the nuclear starburst region of M 83 is the origin of the global correlation on a galactic (a few kpc) scale shown by Gao & Solomon (2004a). In other words, $R_{\text{HCN/CO}}$ (dense gas fraction) and SFE on a galactic scale are averages of those parameters on a GMA scale. Low- $R_{\text{HCN/CO}}$ (less dense) GMAs would be dominant in a low-SFE galaxy, whereas high- $R_{\text{HCN/CO}}$ (dense) GMAs are possibly dominant in a high-SFE galaxy. This is consistent with the prediction of a three-dimensional, high-resolution hydrodynamic simulation (Wada & Norman 2007). They showed the SFR and SFE are sensitive to increasing average density of molecular gas. The average gas density just corresponds to $R_{\text{HCN/CO}}$.

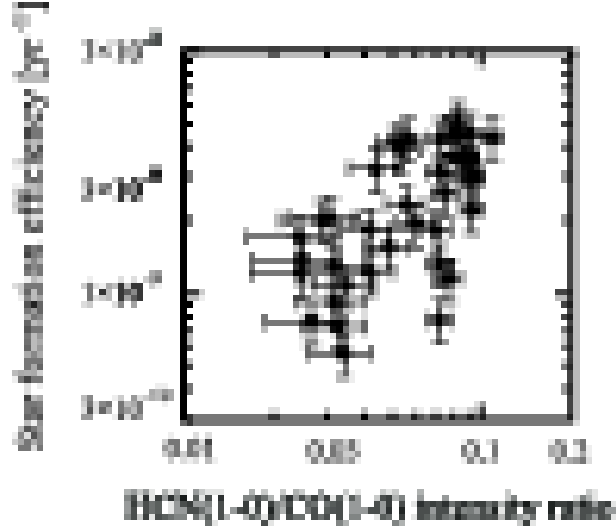


Fig. 12. A plot of $R_{\text{HCN/CO}}$ vs. SFE in the central region of M 83. The correlation between $R_{\text{HCN/CO}}$ and the SFE is clearly seen in $7''.5 \times 7''.5$ ($160 \text{ pc} \times 160 \text{ pc}$) scale.

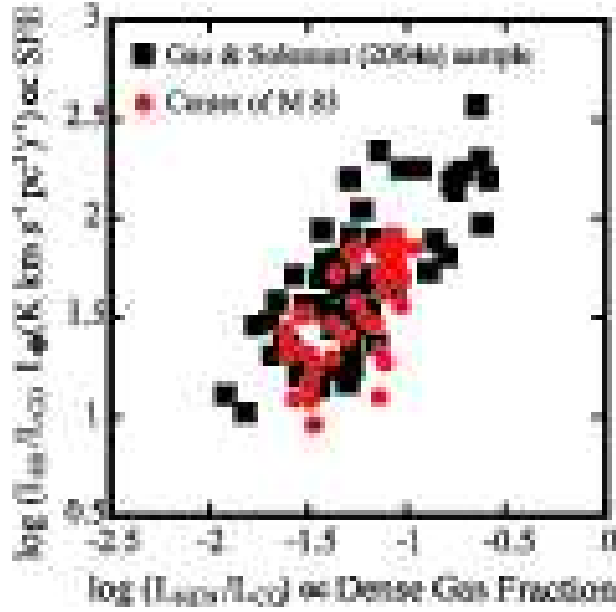


Fig. 13. A composite of the $R_{\text{HCN/CO}}$ vs. SFE plots for the central region of M 83 (this work) and for ULIRGs, LIRGs, and normal spirals (Gao & Solomon 2004a). The distances of the Gao & Solomon (2004a) sample are in the range of 2.5 Mpc to 266 Mpc. Black squares indicate the Gao & Solomon (2004a) sample, and red circles indicate the center of M 83. The correlation between $R_{\text{HCN/CO}}$ and the SFE in the central region of M 83 almost seems to coincide with that of the Gao & Solomon (2004a) sample.

5. Summary

We have performed aperture synthesis high-resolution ($\sim 7'' \times 3''$) observations in the CO($J = 1 - 0$) line, the HCN($J = 1 - 0$) line, and the 95 GHz continuum emission toward the central region (~ 1.5 kpc) of the nearby barred spiral galaxy M 83 with the NMA. A summary of this work is as follows.

1. The size of the CO($J = 1 - 0$) map is $2' \times 1'$ (3 pointings mosaic observations). The synthesized beam size and the resultant rms noise level of the intensity map are $7'' \times 3''$ and $2.7 \text{ Jy beam}^{-1} \text{ km s}^{-1}$, respectively. Our high resolution CO($J = 1 - 0$) mosaic map with the highest sensitivity and the highest spatial resolution to date depicts the presence of molecular ridges along the leading sides of the stellar bar and nuclear twin peak structure. In addition, we combined the NMA CO($J = 1 - 0$) data with the NRO 45-m CO($J = 1 - 0$) data. The combined CO($J = 1 - 0$) map first reveals the high-resolution distribution of molecular gas containing diffuse components in the central region of M 83.
2. The size of the HCN($J = 1 - 0$) map and the 95 GHz continuum map is $77''$. The synthesized beam size is $7'' \times 3''$ for the HCN($J = 1 - 0$) map and $8'' \times 3''$ for the 95 GHz continuum map, respectively. The resultant noise level is $0.52 \text{ Jy beam}^{-1} \text{ km s}^{-1}$ for the HCN($J = 1 - 0$) intensity map and $0.85 \text{ mJy beam}^{-1}$ for 95 GHz continuum map, respectively. We found the distribution of the HCN($J = 1 - 0$) line emission which traces dense molecular gas shows nuclear single peak structure, and coincides well with that of the 95 GHz continuum emission which traces massive starburst. However, the peaks of the HCN($J = 1 - 0$) line and the 95 GHz continuum emission are not associated with the optical starburst traced by the HST V-band image.
3. Using the H α /Pa α ratio, an extinction map of the center of M 83 is obtained. The highest extinction is $A_{\text{H}\alpha} \sim 4 \text{ mag}$ ($A_V \sim 5 \text{ mag}$), and which is spatially coincides with the peak of extinction-corrected H α luminosity and that of the HCN($J = 1 - 0$) line emission. This suggests the existence of deeply buried ongoing starburst due to strong extinction near the peaks of the HCN($J = 1 - 0$) line and the 95 GHz continuum emission.
4. We found that $R_{\text{HCN/CO}}$ correlates well with the extinction-corrected SFE using the MIPS $24 \mu\text{m}$ data in the central region of M 83 at a resolution of $7''.5$ ($\sim 160 \text{ pc}$). That is, the SFE is controlled by dense gas fraction traced by $R_{\text{HCN/CO}}$ on a GMA scale. In addition, the correlation between $R_{\text{HCN/CO}}$ and the SFE in the central region of M 83 seems to be almost coincident with that of Gao & Solomon (2004a) sample. This suggests that the correlation between $R_{\text{HCN/CO}}$ and the SFE on a GMA ($\sim 160 \text{ pc}$) scale found in the nuclear starburst region of M 83 is the origin of the global correlation on a few kpc scale shown by Gao & Solomon (2004a).

We would like to acknowledge the referee for his invaluable comments. We are deeply

indebted to the NRO staff for the operation of the telescopes and their continuous efforts to improve the performance of the instruments. We are grateful to F. Comerón for sending us the V-band image of M 83 obtained with VLT, M. Fukuhara for providing us his CO($J = 1 - 0$) image obtained with the NRO 45-m telescope, and A. Hirota for his HCN($J = 1 - 0$) data obtained with the NRO 45-m. K. M. was financially supported by a Grant-in-Aid for JSPS Fellows. This study was partly supported by the MEXT Grant-in-Aid for Scientific Research on Priority Areas No. 15071202. This research has made use of the NASA/IPAC Extragalactic Database (NED) which is operated by the Jet Propulsion Laboratory, California Institute of Technology, under contract with the National Aeronautics and Space Administration. This work is based on observations made with the NASA/ESA Hubble Space Telescope, obtained from the data archive at the Space Telescope Science Institute. STScI is operated by the Association of Universities for Research in Astronomy, Inc. under NASA contract NAS 5-26555. This work is based on observations made with the Spitzer Space Telescope, which is operated by the Jet Propulsion Laboratory, California Institute of Technology under a contract with NASA.

References

- Bayet, E., Gerin, M., Phillips, T. G., & Contursi, A. 2006, *A&A*, 460, 467
- Calzetti, D., et al. 2007, *ApJ*, 666, 870
- Carilli, C. L., et al. 2005, *ApJ*, 618, 586
- Comerón, F. 2001, *A&A*, 365, 417
- Condon, J. J. 1992, *ARA&A*, 30, 575
- Dame, T. M., Hartmann, D., & Thaddeus, P. 2001, *ApJ*, 547, 792
- Díaz, R. J., Dottori, H., Aguero, M. P., Mediavilla, E., Rodrigues, I., & Mast, D. 2006, *ApJ*, 652, 1122
- Dumke, M., Nieten, C., Thuma, G., Wielebinski, R., & Walsh, W. 2001, *A&A*, 373, 853
- Fathi, K., et al. 2008, *ApJL*, 675, L17
- Gao, Y., & Solomon, P. M. 2004a, *ApJ*, 606, 271
- Gao, Y., & Solomon, P. M. 2004b, *ApJS*, 152, 63
- Graciá-Carpio, J., García-Burillo, S., Planesas, P., Fuente, A., & Usero, A. 2008, *A&A*, 479, 703
- Handa, T., Nakai, N., Sofue, Y., Hayashi, M., & Fujimoto, M. 1990, *PASJ*, 42, 1
- Handa, T., Ishizuki, S., & Kawabe, R. 1994, *IAU Colloq. 140: Astronomy with Millimeter and Submillimeter Wave Interferometry*, 59, 341
- Harris, J., Calzetti, D., Gallagher, J. S., III, Conselice, C. J., & Smith, D. A. 2001, *AJ*, 122, 3046
- Helfer, T. T., & Blitz, L. 1997a, *ApJ*, 478, 162
- Ho, L. C., Filippenko, A. V., & Sargent, W. L. W. 1997, *ApJ*, 487, 579
- Houghton, R. C. W., & Thatte, N. 2008, *MNRAS*, 385, 1110
- Ishizuki, S. 1993, Ph.D. Thesis
- Israel, F. P., & Baas, F. 2001, *A&A*, 371, 433
- Jarrett, T. H., Chester, T., Cutri, R., Schneider, S. E., & Huchra, J. P. 2003, *AJ*, 125, 525
- Jogee, S., Scoville, N., & Kenney, J. D. P. 2005, *ApJ*, 630, 837

- Kennicutt, R. C., Jr. 1998a, *ApJ*, 498, 541
- Kennicutt, R. C., Jr. 1998b, *ARA&A*, 36, 189
- Kohno, K., Ishizuki, S., Okayasu, R., Okuda, T., Tosaki, T., & Kawabe, R. 2008b, *PASJ*, submitted
- Kohno, K., Kawabe, R., & Vila-Vilaró, B. 1999, *ApJ*, 511, 157
- Kohno, K., Nakanishi, K., Tosaki, T., Muraoka, K., Miura, R., Ezawa, H., & Kawabe, R. 2008a, *Ap&SS*, 313, 279
- Kohno, K., Tosaki, T., Matsushita, S., Vila-Vilaó, B., Shibatsuka, T., & Kawabe, R. 2002, *PASJ*, 54, 541
- Kuno, N., et al. 2007, *PASJ*, 59, 117
- Lundgren, A. A., Wiklind, T., Olofsson, H., & Rydbeck, G. 2004, *A&A*, 413, 505
- Meurer, G. R., et al. 2006, *ApJS*, 165, 307
- Muraoka, K., et al. 2007, *PASJ*, 59, 43
- Neininger, N., Beck, R., Sukumar, S., & Allen, R. J. 1993, *A&A*, 274, 687
- Okumura, S. K., et al. 2000, *PASJ*, 52, 393
- Osterbrock, D. E., & Ferland, G. J. 2006, *Astrophysics of gaseous nebulae and active galactic nuclei*, 2nd. ed. by D.E. Osterbrock and G.J. Ferland. Sausalito, CA: University Science Books, 2006,
- Petitpas, G. R., & Wilson, C. D. 1998, *ApJ*, 503, 219
- Riechers, D. A., Walter, F., Carilli, C. L., & Bertoldi, F. 2007, *ApJL*, 671, L13
- Ryder, S. D., Sharp, R. G., Knapen, J. H., Mazzuca, L. M., & Parry, I. R. 2005, *The Evolution of Starbursts*, 783, 155
- Sakamoto, K., Matsushita, S., Peck, A. B., Wiedner, M. C., & Iono, D. 2004, *ApJL*, 616, L59
- Sault, R. J., Teuben, P. J., & Wright, M. C. H. 1995, *Astronomical Data Analysis Software and Systems IV*, 77, 433
- Scoville, N. Z., & Sanders, D. B. 1987, *Interstellar Processes*, 134, 21
- Shibatsuka, T., Matsushita, S., Kohno, K., & Kawabe, R. 2003, *PASJ*, 55, 87
- Solomon, P. M., Downes, D., & Radford, S. J. E. 1992, *ApJL*, 387, L55
- Soria, R., & Wu, K. 2002, *A&A*, 384, 99
- Thatte, N., Tecza, M., & Genzel, R. 2000, *A&A*, 364, L47
- Thim, F., Tammann, G. A., Saha, A., Dolphin, A., Sandage, A., Tolstoy, E., & Labhardt, L. 2003, *ApJ*, 590, 256
- Tsutsumi, T., Morita, K.-I., & Umeyama, S. 1997, *Astronomical Data Analysis Software and Systems VI*, 125, 50
- Wada, K., & Norman, C. A. 2007, *ApJ*, 660, 276
- Wall, W. F. 1991, Ph.D. Thesis
- Wu, J., Evans, N. J., II, Gao, Y., Solomon, P. M., Shirley, Y. L., & Vanden Bout, P. A. 2005, *ApJL*, 635, L173
- Young, J. S., Allen, L., Kenney, J. D. P., Lesser, A., & Rownd, B. 1996, *AJ*, 112, 1903